Gust Load Alleviation Control of Aircraft with Varying Mass Distribution

Matthias Wüstenhagen

Today's aviation research intensively examines new materials and high aspect ratio wings. These advances in aircraft design demand for secondary control algorithms supporting the aircraft structure. As a novel approach, this paper discusses model predictive control as augmentation to a long-range aircraft with increased vulnerability to gust encounter. Model predictive control provides the possibility to directly control the parameter of interest in the presence of constraints. The proposed gust load alleviation control method processes estimates of the wing root bending moment. The control surface deflections chosen to fulfill this task are limited in deflection and rate. Gust load alleviation controllers are synthesised for different mass cases and flight conditions. Subsequently, the most critical loads over the wing span are identified with and without gust load alleviation.

Wüstenhagen, M. "Gust Load Alleviation Control of Aircraft with Varying Mass Distribution," *AIAA Scitech 2023 Forum*, American Institute of Aeronautics and Astronautics, National Harbor, Maryland, 2023. https://doi.org/10.2514/6.2023-0371

Gust Load Alleviation Control of Aircraft with Varying Mass Distribution

Matthias Wüstenhagen*
German Aerospace Center (DLR), 82234 Weßling, Germany

Today's aviation research intensively examines new materials and high aspect ratio wings. These advances in aircraft design demand for secondary control algorithms supporting the aircraft structure. As a novel approach, this paper discusses model predictive control as augmentation to a long-range aircraft with increased vulnerability to gust encounter. Model predictive control provides the possibility to directly control the parameter of interest in the presence of constraints. The proposed gust load alleviation control method processes estimates of the wing root bending moment. The control surface deflections chosen to fulfill this task are limited in deflection and rate. Gust load alleviation controllers are synthesised for different mass cases and flight conditions. Subsequently, the most critical loads over the wing span are identified with and without gust load alleviation.

I. Introduction

Commercial aviation contributes between 3 to 5 % to the global warming through the emission of carbon dioxide (CO_2) and nitrogen oxide (NO_x) as well as through cirrus cloud formation caused by contrails [1]. Due to the expected growth rate of annual air transport demand of approximately 4.5 % until the year 2050, advances in the fuel efficiency of aircraft are ecologically indispensable [2]. Moreover, airlines strive to operate more fuel-efficient aircraft also from an economical point of view. The direct operating costs of today's aircraft strongly depend on the oil price which makes aircraft designs with a comparatively low kerosene consumption favourable [1]. Different possibilities in aviation research are being examined with respect to their fuel saving potential. They range from new aircraft configurations, like the blended-wing body, over increased propulsion efficiency, to the application of lightweight materials and structures as well as high aspect ratio wings. Combining lightweight wing structures with higher aspect ratios raises the lift-to-drag quotient as the induced drag decreases. This kind of modification to aircraft design holds a crucial potential to enhance the fuel efficiency and make flying more economically and ecologically attractive [1]. However, these wings tend to be more flexible which makes unstable phenomena like flutter more likely to occur and increases the demand for active flutter suppression (AFS) [3]. Moreover, these aircraft are more vulnerable to manoeuvre and gust loads [4, 5]. Passive and active load alleviation methods help to reduce critical loads acting on the wing structure. Active methods can be used for manoeuvre load alleviation (MLA) and gust load alleviation (GLA) [6–9]. The available control surfaces are deployed for MLA and GLA. With active MLA the lift is shifted more inboard to reduce the wing bending during manoeuvres. Active GLA, on the other hand, aims at minimising the peak loads and the perturbation in the aircraft rigid body motion [10]. The synthesis of MLA or GLA controllers is a demanding problem as high-aspect-ratio-aircraft lack a clear separation of rigid body and flexible modes [5]. Within the scope of this paper, the focus is on reducing the bending loads with GLA.

Several control strategies have been considered for GLA. In Ref. [11] a controller with static feedback is synthesised to perform GLA and AFS by pole placement. Static feeback control is also proposed in Ref. [12]. A linear quadratic optimal controller for GLA and MLA is used by Ref. [13] to alleviate the wing bending moment (BM). In contrast, Ref. [14] proposes a linear quadratic Gaussian regulator (LQG) to reduce the structural displacement. Using measurements of a light detection and ranging (LIDAR) sensor, which detects turbulence ahead of aircraft and therefore enables a faster reaction time to approaching gusts, is considered in several publications [15–19]. Feedforward control can be applied with LIDAR. Ref. [15] additionally uses an adaptive control method in order to adapt to changes in the structural dynamics of aircraft. Quite popular is the application of $\mathcal{H}_\infty$ methods [6, 9, 17, 19, 20]. These aim at reducing the $\mathcal{H}_\infty$ norm of transfer functions within a certain frequency range [21]. Model predictive control (MPC), on the other hand, solves an optimisation problem online. This is done repeatedly at a certain frequency [22]. Applying MPC for load alleviation has been proposed by Refs. [16, 23–25]. MPC has the advantage of taking constraints for inputs, states

*Research Fellow, Institute of System Dynamics and Control, Münchener Straße 20, 82234 Weßling

and outputs into consideration, while at the same time, optimising a performance criterion online, e.g. the wing root bending moment (WRBM).

Due to these advantages, MPC is applied in the GLA control for a long-range aircraft in this paper. Vertical 1-cosine gust encounters for nine mass cases in three different flight conditions are taken into account. As an air data boom is assumed to be mounted at the aircraft nose, angle of attack measurements allow feedforward control. Measurements provided by inertial measurement units (IMUs) located on the wings and the fuselage are fed back to the MPC unit as well. The GLA control mainly aims at minimising the estimated wing WRBM.

Firstly, the aeroservoelastic modelling process is described in Section II. An introduction to MPC theory is given in Section III. Finally, Section IV summarises the results of the GLA controller synthesis with MPC.

II. Aeroservoelastic Aircraft Model

Within the scope of this paper, the considered dynamic system is a generic long-range aircraft model which encounters gusts during flight. In a first step, an open-loop, aeroservoelastic model of the aircraft is set up. Like shown in Fig. 1, it involves the coupling between the aerodynamics and structural dynamics, as well as actuators of the control surfaces and sensors. In a subsequent step, the control system can be synthesised, which is represented by the GLA

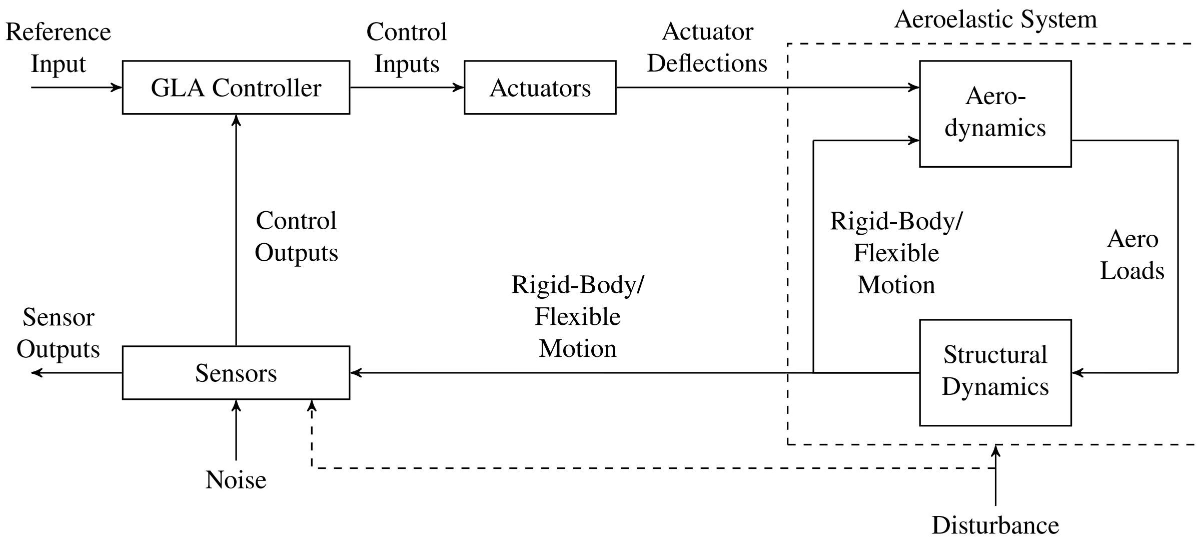

Fig. 1 Aeroservoelastic system [26].

controller.

A. Aeroelastic Model

A finite element (FE) model shapes the structural model which is condensed with the Guyan reduction [27]. The red points in Fig. 2 indicate the nodes of the structural grid for the reference aircraft. Under the assumptions listed in Ref. [9], the subsequent equations of motion (EOMs) can be applied. The non-linear Newton-Euler EOM

$$\begin{bmatrix} m_b(\dot{V}_b + \Omega_b \times V_b - T_{be}(\Theta_b) g_e) \\ J_b \dot{\Omega}_b + \Omega_b \times (J_b \Omega_b) \end{bmatrix} = \underbrace{\Phi_{gb}^T P_g^{\text{ext}}}_{P_b^{\text{ext}}} \tag{1}$$

introduces the rigid body flight mechanics. The translational and angular velocities of the aircraft are V_b and Ω_b in the body frame of reference. The vector g_e is the gravitational acceleration transformed by $T_{be}(\Theta_b)$ from the earth fixed to the body fixed frame of reference, where Θ_b represents the Euler angles. The external load vector P_g^{ext}, containing contributions on each structural grid point, converts with matrix Φ_{gb}^T to loads on the rigid body motion [28, 29]. The

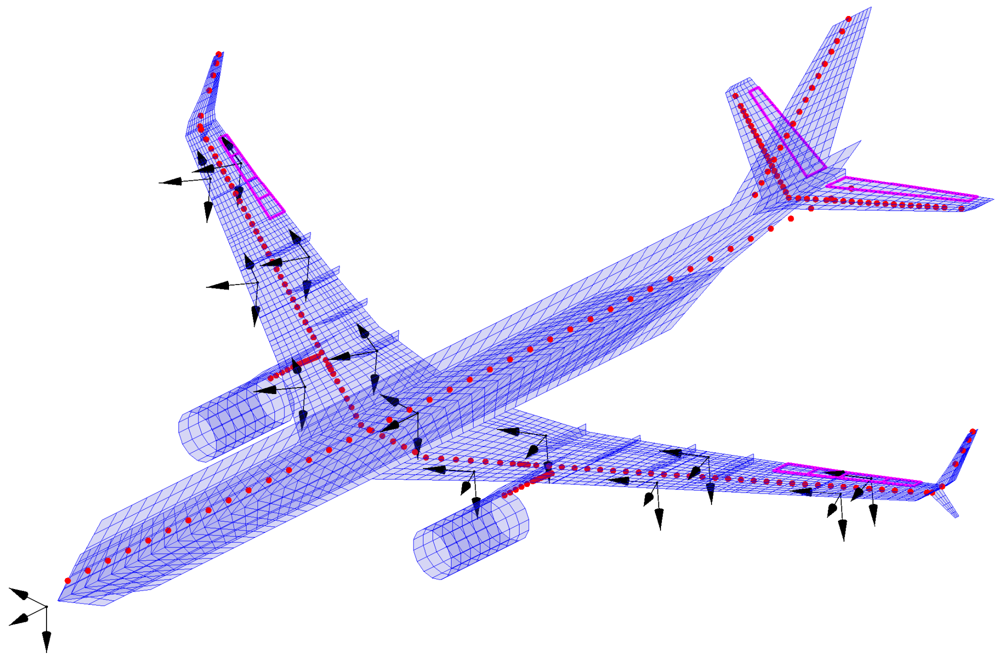

Fig. 2 Reference flexible aircraft model defined by the structural grid (red), the aerodynamic panel model (blue), the deployed control surfaces for GLA (magenta) and the sensor coordinate system locations and orientations (black).

flexible motion of the aircraft structure is described by linear elastic theory with

$$M_{ff}\ddot{u}_f + B_{ff}\dot{u}_f + K_{ff}u_f = \underbrace{\Phi_{gf}^T P_g^{\text{ext}}(t)}_{P_f^{\text{ext}}(t)}, \tag{2}$$

where the generalised displacement vector u_f and its first and second derivatives $\dot{u}_f$ and $\ddot{u}_f$ are multiplied with the modal mass, damping and stiffness matrices M_{ff}, B_{ff} and K_{ff}. The modal matrix Φ_{gf} on the right-hand side contains the eigenvectors of the structural modes sorted by frequency [28]. Modal truncation allows to reduce the DOFs for the most relevant eigenmodes [29].
The external loads P_g^{ext} combine the thrust and aerodynamic loads P_g^{eng} and P_g^{aero} yielding

$$P_g^{\text{ext}} = P_g^{\text{eng}} + P_g^{\text{aero}}. \tag{3}$$

The aerodynamic loads are determined with the doublet lattice method (DLM) combining steady and unsteady aerodynamic effects. As can be seen in Fig. 2, the lifting surfaces of the demonstrator aircraft are discretised by trapezoid panels. Doublets are located at the quarter-chord line of each panel. In the reduced frequency domain k, the pressure coefficients fulfilling the Pistolesi Theorem at the 3/4-chord line j are

$$\Delta c_{pj}(k) = Q_{jj}(k)w_j(k), \tag{4}$$

where the matrix $Q_{jj}(k)$ contains the aerodynamic influence coefficients (AICs) and $w_j(k)$ the downwash. The reduced frequency is

$$k = \omega\frac{c_r}{2U_\infty}. \tag{5}$$

In Equation (5), ω depicts the modal frequency, while c_r represents the length of the reference chord. For $k = 0$ the pressure coefficient $\Delta c_{pj}(0)$ only includes quasi-steady aerodynamic effects. The AIC matrix is approximated with Roger's method in the time domain. Thereby, the lag states x_l are introduced due to the unsteady aerodynamics [28, 30]. The downwash w_j is affected by different contributions leading to

$$w_j = w_{j,b_1} + w_{j,\text{cs}_0} + w_{j,\text{cs}_1} + w_{j,f_0} + w_{j,f_1} + w_{j,t_1}. \tag{6}$$

The first term w_{j,b_1} results from the rigid body velocity V_b and angular velocity Ω_b. The control surface deflections u_{cs} and deflection rates $\dot{u}_{\text{cs}}$ induce the contributions w_{j,cs_0} and w_{j,cs_1}. The flexible motion with modal deflection u_f and its derivative $\dot{u}_f$ result in w_{j,f_0} and w_{j,f_1}. Finally, w_{j,t_1} comes from gusts and atmospheric turbulence. Detailed information on how the contributions are determined is found in Refs. [28, 31].
The structural dynamics affect the downwash w_j and thereby the aerodynamics. The effect from the aerodynamics on the structural dynamics comes from the aerodynamic loads P_g^{aero} closing the aeroelastic loop as stated in Fig. 1. The aerodynamic loads on the structural grid are

$$P_g^{\text{aero}} = q_\infty T_{kg}^T S_{kj} Q_{jj} w_j. \tag{7}$$

The matrix S_{kj} multiplies each pressure coefficient at the 3/4-point j with the area of the corresponding aerodynamic box and transforms it to the centre point k. The transpose of the spline matrix T_{kg} projects the contributions of the aerodynamic boxes on the structural grid. Finally, multiplication with the dynamic pressure q_∞ yields the aerodynamic loads on the aircraft structure. They cause a rigid and flexible body motion of the aircraft structure which, in turn, affects the aerodynamics [26, 28, 29].
Further details on the structural and aerodynamic modelling approach are given in Refs. [9, 29, 31].

B. Gust Model

Within the scope of this paper, the atmospheric disturbance comes from different vertical 1-cosine gust profiles. They are defined by the gust zone velocity and acceleration $U_{z,t}(t)$ and $\dot{U}_{z,t}(t)$

$$\begin{aligned} U_{z,t}(t) &= \begin{cases} \frac{\bar{U}_t}{2}\left(1-\cos\left(\frac{\pi}{H_t}\left(U_\infty t - x_z\right)\right)\right), & \text{if } \frac{x_z}{U_\infty} \le t \le \frac{2H_t + x_z}{U_\infty} \\ 0, & \text{otherwise} \end{cases} \\ \dot{U}_{z,t}(t) &= \begin{cases} \frac{\bar{U}_t \pi}{2H_t} U_\infty \sin\left(\frac{\pi}{H_t}\left(U_\infty t - x_z\right)\right), & \text{if } \frac{x_z}{U_\infty} \le t \le \frac{2H_t + x_z}{U_\infty} \\ 0, & \text{otherwise.} \end{cases} \end{aligned} \tag{8}$$

The maximum gust intensity and gust half length are $\bar{U}_t$ and H_t [32]. As time t passes the aircraft moves through the gust from nose to aft, like shown in Fig. 3. The aerodynamic model of the reference aircraft is separated in ten gust

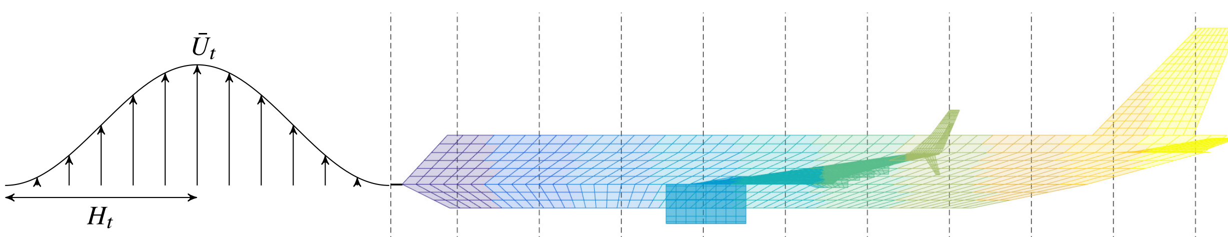

Fig. 3 1-cosine gust and aircraft gust zones.

zones as indicated by the different colours of the panels. All aerodynamic panels within a gust zone are affected by the gust velocity observed at the centre line at position x_z, which is indicated by the dashed vertical lines. Namely, within a gust zone the gust velocity is constant. The air data boom at the nose of the aircraft is specially treated by introducing another gust zone. Thus, changes in the angle of attack α, due to an approaching gust, are recognised before it hits the aircraft. When it comes to GLA control this offers the opportunity to use a feedforward path decreasing the reaction time [21]. The gust zone approach is an approximation which saves a lot of computation time as it groups many aerodynamic panels into few zones. With ten gust zones the implementation was found to be accurate enough [33]. The difference in the gust zone velocity of two neighbouring gust zones can be considered by a time delay depending on the airspeed U_∞. The transfer function of a time delay is

$$G_{z,d}(s) = e^{-t_{z,d}s}, \tag{9}$$

where $t_{z,d}$ is the time delay in seconds and s is the Laplace variable [33]. Equation (9) is approximated by a second-order Padé approximation

$$G_{z,d}(s) \approx \frac{s^2 - \frac{6}{t_{z,d}} s + \frac{12}{t_{z,d}^2}}{s^2 + \frac{6}{t_{z,d}} s + \frac{12}{t_{z,d}^2}} \tag{10}$$

as it is convertible into a linear state-space system with the additional states $x_{z,d}$ [34]. Thus, it is possible to combine the inputs to all gust zones in two inputs $U_{z,g}$ and $\dot{U}_{z,g}$ at the air data boom. A gust then propagates through time delay over all gust zones.

C. Sensor Model

Sensors are attached at different positions along the aircraft. Their measurements are available to the GLA controller or can be used for performance analysis. In Fig. 2 the sensor locations and orientations are indicated by the coordinate systems. The coordinate system in front of the aircraft nose corresponds to the air data boom. It provides the pressure, the altitude h_a, the indicated airspeed $U_{\mathrm{IAS},a}$, the angle of attack α_a and the angle of sideslip β_a. The airflow velocity vector V_a at the air data boom is given by

$$V_a = \begin{bmatrix} u_a \\ v_a \\ w_a \end{bmatrix} = V_b + \Omega_b \times \left(r_{ab} + T_{af} \Phi_{gf} u_f\right) + T_{af} \dot{u}_f + V_t, \tag{11}$$

where u_a, v_a and w_a are the velocity contributions with respect to the air data boom coordinate system [35]. The first term on the right side outlines the centre of gravity (CG) velocity. As the orientation of the body and air data boom coordinate system coincide, a transformation is not necessary. The second term represents the velocity caused by the rotation of the rigid body Ω_b and the lever arm joining the CG and the air data boom position. Thus, the vector r_{ab} describes the distance between the CG and the air data boom position on the undeformed aircraft structure. The second contribution enclosed by the parentheses adds the structural deformation, which is transformed by T_{af} from the flexible frame of reference to the air data boom frame of reference. The third term of Equation (11) denotes the flexible velocity recorded at the air data boom. Finally, V_t adds the velocity provoked by turbulence. In case of a discrete and upwards vertical 1-cosine gust, as considered within the scope of this paper, the time dependent V_t is

$$V_t(t) = \begin{bmatrix} 0 \\ 0 \\ -U_{z,t}(t) \end{bmatrix}. \tag{12}$$

The gust velocity $U_{z,t}(t)$ at the position of the air data boom is defined in Equation (8). The indicated airspeed, as measured by the air data boom, is

$$U_{\mathrm{IAS},a} = a_0 \sqrt{\frac{2}{\kappa - 1}\left(\left(\frac{q_{\infty,a}}{p_0} + 1\right)^{(\kappa-1)/\kappa} - 1\right)} \tag{13}$$

with the speed of sound at mean sea level a_0, the heat capacity ratio κ, the static pressure at mean sea level p_0 and the dynamic pressure $q_{\infty,a}$ experienced at the air data boom. The dynamic pressure $q_{\infty,a}$ is

$$q_{\infty,a} = p\left(\left(\frac{\kappa - 1}{2} \frac{(u_a^2 + v_a^2 + w_a^2)}{a^2} + 1\right)^{\kappa/(\kappa-1)} - 1\right), \tag{14}$$

where p is the static pressure and a is the speed of sound [36].
By means of Equation (11), the angle of attack α_a and the angle of sideslip β_a are reconstructed by

$$\alpha_a = \arctan\left(\frac{w_a}{u_a}\right) \tag{15}$$

and

$$\beta_a = \arcsin\left(\frac{w_a}{\sqrt{u_a^2 + v_a^2 + w_a^2}}\right) \tag{16}$$

at the air data boom [35].
IMUs record the translational accelerations and the rotational rates. With reference to Fig. 2, 13 IMUs are distributed over the aircraft structure. In order to have a clearer picture on the aeroelastic behaviour of the wings, six IMUs are placed along arbitrarily defined front and rear spar lines on both wings. The wing IMUs are tilted with respect to the body frame of reference as they are aligned with the spars and the wing dihedral. One IMU is located close to the CG and aligns with the body frame of reference. The translational acceleration at the position of the IMUs with respect to the body frame of reference is

$$\begin{aligned}\ddot{u}_{\mathrm{trans},s,b} = &\underbrace{\dot{V}_b + \Omega_b \times V_b}_{1} + \underbrace{2\Omega_b \times T_{\mathrm{trans},bf}\,\dot{u}_f}_{2} + \underbrace{T_{\mathrm{trans},bf}\,\ddot{u}_f}_{3} \\ &+ \underbrace{\dot{\Omega}_b \times (r_{sb,b} + T_{\mathrm{trans},bf}\,u_f)}_{4} + \underbrace{\Omega_b \times \left(\Omega_b \times (r_{sb,b} + T_{\mathrm{trans},bf}\,u_f)\right)}_{5} - \underbrace{T_{be}(\Theta_b) g_e}_{6} .\end{aligned} \tag{17}$$

The six contributions represent the acceleration of the aircraft CG (1), the Coriolis acceleration (2), the modal acceleration (3), the tangential acceleration (4), the centrifugal acceleration (5) and the gravitational acceleration (6). The transformation matrix $T_{\mathrm{trans},bf}$ converts motion from the modal to the body frame of reference. The vector $r_{sb,b}$ defines the rigid part of the vector connecting the CG and the position of the corresponding IMU. One final transformation from the body frame of reference to the sensor coordinate system would yield the translational acceleration observed by the IMU. The rotational rates recorded are determined by

$$\dot{u}_{\mathrm{rot},s,b} = \Omega_b + T_{\mathrm{rot},bf}\,\dot{u}_f . \tag{18}$$

Again, Equation (18) is given in the body frame of reference. The transformation matrix $T_{\mathrm{rot},bf}$ converts rotational contributions from modal space into the body frame of reference [35].
The measurements coming from the air data boom and the IMUs exhibit a small time delay, which is represented by a Padé approximation leading to the additional states $x_{a,d}$ and $x_{s,d}$.

D. Loads Model

Load measurements are assumed to be unavailable and therefore can not be directly fed into the GLA controller. However, the performance of a GLA controller is judged by the loads P_c, which the wing structure experiences during gust encounter. Especially the BM $P_{c,\mathrm{mx}}$ is of interest. The loads are estimated using the force summation method (FSM):

$$P_c = T_{cg}\left(P_g^{\mathrm{ext}} - \underbrace{M_{gg}\begin{bmatrix}\Phi_{gb} & \Phi_{gf}\end{bmatrix}\begin{bmatrix}\ddot{u}_b \\ \ddot{u}_f\end{bmatrix}}_{P_g^{\mathrm{iner}}}\right) \tag{19}$$

with the external and inertial loads P_g^{ext} and P_g^{iner}. The mass matrix M_{gg} is defined according to the structural grid. The rigid body acceleration $\ddot{u}_b$ is

$$\ddot{u}_b = \begin{bmatrix}\dot{V}_b + \Omega_b \times V_b - T_{be}(\Theta_b) g_e \\ \dot{\Omega}_b + J_b^{-1}(\Omega_b \times (J_b \Omega_b))\end{bmatrix} . \tag{20}$$

By means of the matrix T_{cg}, the incremental loads of all grid points from the wing tip up to the considered wing position are summed up and transformed to the loads coordinate system [28, 37].

E. Integrated Model

Eventually, the model components can be combined to an aeroservoelastic model. The actuators of the control surfaces are transfer functions of order 2 and will not be discussed in detail. The outputs y of the aeroservoelastic model comprise the measurements of the previously mentioned sensors and wing loads necessary for performance assessment. Finally, the aircraft model can be described by

$$\begin{aligned}\dot{x}(t) &= f(x(t), u(t)) \\ y(t) &= g(x(t), u(t))\end{aligned} \tag{21}$$

as a state-space model [21]. The time dependent states, inputs and outputs are

$$x = \begin{bmatrix} V_b \\ \Omega_b \\ R_b \\ \Theta_b \\ u_f \\ \dot{u}_f \\ u_{\text{cs}} \\ \dot{u}_{\text{cs}} \\ x_{z,d} \\ x_{a,d} \\ x_{s,d} \\ x_l \end{bmatrix}, \quad u = \begin{bmatrix} u_{\text{cs,cmd}} \\ U_t \\ \dot{U}_t \end{bmatrix}, \quad y = \begin{bmatrix} U_{\text{IAS},a} \\ \alpha_a \\ \beta_a \\ \ddot{u}_{\text{trans},s,b} \\ \dot{u}_{\text{rot},s,b} \\ P_c \end{bmatrix}. \tag{22}$$

The vector R_b describes the position of the aircraft with respect to the inertial system. The command to the control surface actuators are defined by $u_{\text{cs,cmd}}$. Equation (21) describes a non-linear state-space model. Its variables x, u and y can be split into a constant and variable part with

$$x(t) = x^* + \delta x(t), \quad u(t) = u^* + \delta u(t), \quad y(t) = y^* + \delta y(t). \tag{23}$$

The variables with superscript * are constant and indicate the predominant flight condition, while the variables with prepended δ represent time varying deviations from the flight condition [21]. Under the assumption of moderate changes the non-linear state-space model can be linearised yielding the linear time-invariant (LTI) state-space system

$$\begin{aligned} \frac{d\delta x}{dt} &= \underbrace{\frac{\partial f(x,u)}{\partial x}}_{A} \delta x + \underbrace{\frac{\partial f(x,u)}{\partial u}}_{B} \delta u \\ \delta y &= \underbrace{\frac{\partial g(x,u)}{\partial x}}_{C} \delta x + \underbrace{\frac{\partial g(x,u)}{\partial u}}_{D} \delta u. \end{aligned} \tag{24}$$

In the remainder of the paper, systems of the form of Equation (24) are considered. Therefore, the prepended δ will be omitted for the deviations in states, inputs and outputs unless stated differently.

The principle of MPC is explained best in discrete time. In order to do so a sampling time Δt_s is selected. Then, Equation (24) transforms into a discrete LTI of the form

$$\begin{aligned} x(k+1) &= A_s x(k) + B_s u(k) \\ y(k) &= C_s x(k) + D_s u(k). \end{aligned} \tag{25}$$

The index k is the count of passed time steps Δt_s [21]. As MPC does not allow any feedthrough from the control inputs $u_{\text{cs,cmd}}$ to any output y, a time delay of length Δt_s is introduced in order to force matrix D_s to be zero. Thereby, an algebraic loop is prevented [38].

III. Model Predictive Control

Within the scope of this paper, MPC is chosen to fulfill the task of reducing gust loads. Subsequently, the process is described in greater depth.

A. Idea of MPC

In Fig. 4 the general principle of MPC is explained. MPC aims at manipulating the system in a way that certain

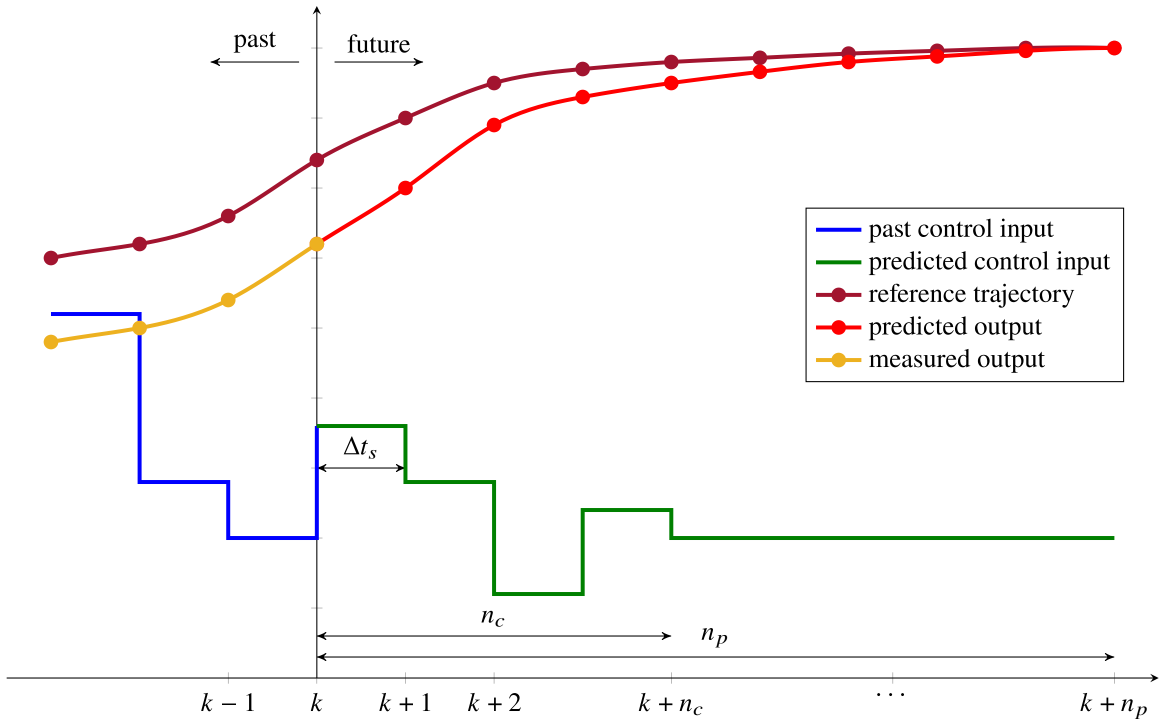

Fig. 4 MPC principle [39].

outputs follow a predefined reference trajectory. By means of a plant model, MPC predicts at time instance k the model output behaviour n_p time steps ahead, where n_p depicts the prediction horizon. It then decides on appropriate input signals to achieve this goal with an optimisation. The change in input signals is determined for n_c time steps into the future and kept constant for time steps between $k + n_c$ and $k + n_p$, i.e. typically the control horizon n_c is smaller than the prediction horizon n_p [40]. Subsequent to the optimisation, MPC applies the first predicted control input increment. As soon as the time step Δt_s has passed and the time instance $k + 1$ is reached, the prediction and control horizon are shifted by one time step and the optimisation repeats [39]. MPC comes with a high computational burden as an optimisation problem is solved online repeatedly. This makes real-time applications challenging. However, as the capability of today's computers increases, MPC becomes more and more appealing [22].

B. State Estimation

In general, the system states are not directly measured and have to be estimated. Moreover, it has to be predicted how changes to the system inputs will affect future plant outputs. A Kalman filter is necessary to fulfill this task. Another option would be to use moving horizon estimation (MHE) as proposed by Refs. [24, 25]. The state observer model in state-space format is

$$\begin{aligned} x_o(k+1) &= A_o x_o(k) + B_o u_o(k) \\ y_o(k) &= C_o x_c(k) + D_o u_o(k). \end{aligned} \tag{26}$$

The observer in Equation (26) is an augmented version of the state-space system of the plant, which additionally incorporates an unmeasured disturbance model, a measurement noise and output disturbance model. The observer states, inputs and outputs are

$$x_o = \begin{bmatrix} x \\ x_t \\ x_d \end{bmatrix}, \quad u_o = \begin{bmatrix} u \\ w_t \\ w_d \\ w_n \end{bmatrix}, \quad y_o = \begin{bmatrix} U_{\mathrm{IAS},a,o} \\ \alpha_{a,o} \\ \beta_{a,o} \\ \ddot{u}_{\mathrm{trans},s,b,o} \\ \dot{u}_{\mathrm{rot},s,b,o} \\ P_{c,o} \end{bmatrix}. \tag{27}$$

In Equation (27) all input variables indicated by w depict white noise. The states and inputs with subscript t correspond to the input disturbance model, that is connected to the gust inputs U_t and $\dot{U}_t$ of the plant model. As it is in general not known what kind of input disturbance will hit the aircraft, the input disturbance model for the observer is assumed to be a step-like response. The states and inputs with subscript d belong to an output disturbance model, which represents integrated white noise and therefore is a step-like response as well. The input w_n adds white measurement noise to the outputs. No additional states are introduced. The output disturbance and measurement noise are introduced only for the measured outputs, i.e. the outputs that are provided by the sensors. Performance outputs, which are necessary for performance assessment of the MPC controllers are included in the output vector y_o, but are not directly affected by disturbance and noise. This is the case for the loads output P_c. The outputs of the observer y_o are the same outputs y as described in Equation (22), except that they have been affected by noise and disturbance. The matrices A_o, B_o, C_o and D_o in Equation (27) combine the plant, noise and measurement models. For further details on their structure and on the individual steps that are performed for state estimation and the output prediction, it is referred to Ref. [40].

C. Online Optimisation Problem

The decision variable to be determined within the optimisation of MPC at time instance k is

$$z_k = \begin{bmatrix} u(k|k) \\ u(k+1|k) \\ \dots \\ u(k+n_p-1|k) \end{bmatrix}. \tag{28}$$

It includes the control action that is proposed at time instance k for the upcoming n_p time steps. The input $u(k+i|k)$ describes the input at time instance $k+i$ determined at time instance k. The cost function, that has to be minimised, is subdivided in two terms leading to

$$\begin{aligned} J(z_k) = & \underbrace{\min_{w_y} \sum_{j=1}^{n_y} \sum_{i=1}^{n_p} \left(w_{y,j} \left(r_j(k+i|k) - y_j(k+i|k)\right)\right)^2}_{J_y(z_k)} \\ & \underbrace{+ \min_{w_{\Delta u}} \sum_{j=1}^{n_u} \sum_{i=1}^{n_c-1} \left(w_{\Delta u,j} \left(u_j(k+i|k) - u_j(k+i-1|k)\right)\right)^2}_{J_{\Delta u}(z_k)}. \end{aligned} \tag{29}$$

The first term $J_y(z_k)$ applies the output reference tracking, where the difference between the j^{th} reference trajectory $r_j(k+i|k)$ and the j^{th} predicted output of the system $y_j(k+i|k)$ is to be minimised within the prediction horizon. The weight $w_{y,j}$ defines how much emphasis is put onto the difference of output j. All $w_{y,j}$ are grouped in w_y. The second term $J_{\Delta u}(z_k)$ puts an increment limit on the j^{th} input between time steps along the entire control horizon n_c. Again, the individual weights $w_{\Delta u,j}$ are collected in $w_{\Delta u}$. One of the biggest advantages of MPC is that it can also incorporate constraints. For the GLA control problem constraints are assumed for the inputs and input increments by

$$\begin{aligned} u_{j,\min} \le u_j(k+i-1|k) \le u_{j,\max} \\ \Delta u_{j,\min} \le \Delta u_j(k+i-1|k) \le \Delta u_{j,\max} \end{aligned} \quad i = 1, 2, ..., n_p \quad j = 1, 2, ..., n_u. \tag{30}$$

The constant values $u_{j,\min}$ and $u_{j,\max}$ depict the minimum and maximum values of the j^{th} input $u_j(k+i-1|k)$ predicted $i-1$ time steps into the future at time instance k. Respectively, the values $\Delta u_{j,\min}$ and $\Delta u_{j,\max}$ represent the same for the input increments.

IV. Gust Load Alleviation with Model Predictive Control

In the following, a GLA controller is synthesised with MPC for the reference aircraft.

A. Set of Linearised Models

Different mass cases, flight conditions and gust half lengths H_t are considered for the reference aircraft. Table 1 depicts the mass cases. They differ in mass properties ranging from the empty to the maximum take-off mass case as

Table 1 Considered mass cases of the reference aircraft.

No.	Definition
1	operating empty mass
2	rear light payload
3	forward light payload
4	rear heavy payload
5	forward heavy payload
6	central heavy payload
7	forward maximum take-off mass
8	rear maximum take-off mass
9	central maximum take-off mass

well as in the CG position, which is located relatively forward, central or rear.
The relevant flight conditions were pinpointed down to three flight speeds U_∞ at different altitudes h, as shown in Table 2. Furthermore, the range of gust half lengths H_t and maximum gust speeds $\bar{U}_t$ needs to be covered. As depicted in Fig.

Table 2 Considered flight conditions of the reference aircraft.

No.	h [m]	U_∞ [m/s]
1	0	170
2	3000	197
3	8300	264

5, H_t and $\bar{U}_t$ depend on each other and also vary with the altitude [32]. Seven combinations of H_t and $\bar{U}_t$, illustrated as vertical dotted lines, are determined for each altitude.
Collecting all possible permutations for nine mass cases and three flight conditions leads to 27 linearised models in the form of Equation (25). For each model seven different gust encounter are considered resulting in 189 essential cases for GLA.
The set of 27 linearised models possesses a high number of states. For the synthesis of MPC controllers the model order is reduced by selecting and allocating the relevant inputs and outputs for GLA. The control surfaces used for GLA are the four ailerons of each wing and the elevators. The control surfaces are highlighted in magenta in Fig. 2. As only vertical gust cases are taken into account and the structural and aerodynamic model are virtually symmetric with respect to its longitudinal axis, symmetric allocation of the control surfaces on the left and right side is possible. The outputs used for GLA control are for now the α_a measurement from the air data boom, the z-accelerations and x-rotational rates taken from the fuselage IMU and the most inner and outer IMUs at the rear spar of each wing. The left and right wing IMU measurements are allocated based on symmetry. Additionally, the WRBM $P_{c,\text{mx}}$ is provided to the MPC as an unmeasured output. MPC then reconstructs its value based on the provided measurements. The last step in model order reduction is performed by balanced reduction, which drops all unnecessary dynamics within the frequency range of

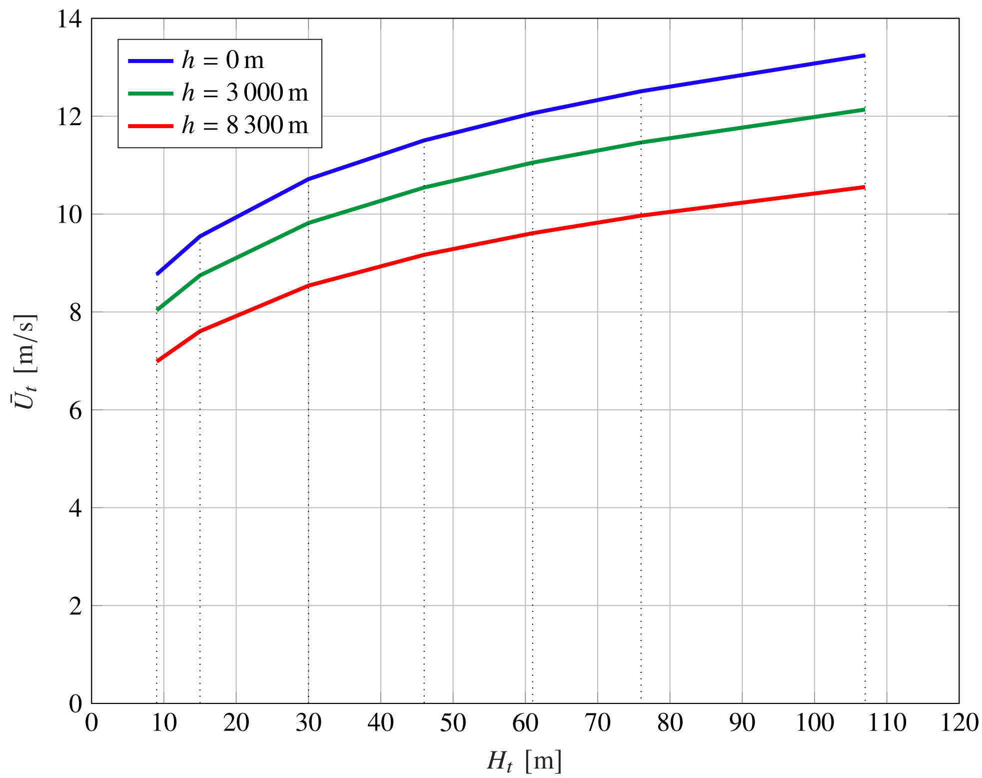

Fig. 5 Maximum gust velocity $\bar{U}_t$ as a function of the gust half length H_t for different altitudes h [32].

interest [41].
Within the scope of this paper, individual controllers for all 27 linearised models are synthesised. It is left to upcoming research activities on how the controllers can be used in unison.

B. Selection of Control Parameters

The sampling time Δt_s, the prediction horizon n_p and the control horizon n_c are kept constant for all 27 models. The sampling time for the MPC controllers was fixed to 0.005 s. Thus, the measurements and control inputs are updated with a frequency of 200 Hz. It was found that increasing the sampling frequency does not lead to a significant performance improvement. Instead, the computational burden would increase.
Trade-offs proved that a prediction horizon $n_p = 100$ and a control horizon of $n_c = 20$ is sufficient to perform GLA. Thereby, the controller predicts the aircraft's behaviour 0.5 s ahead of time and adjusts the control action for the upcoming 0.1 s.
The remaining control parameters to be determined are the weights on the ouputs $w_{y,j}$ and the input increments $w_{\Delta u,j}$. An optimisation was set-up in order to identify their values. The previously defined gust encounters are simulated for each linearised model. The primary goal of GLA control is to reduce the WRBM of the closed-loop system in comparison to the open-loop system. Therefore, the objective function is

$$J(w_y, w_{\Delta u}) = \min_{w_y, w_{\Delta u}} \frac{\max\limits_{i,k}(P_{c,\mathrm{mx,cl},i}(k, w_y, w_{\Delta u})^2)}{\max\limits_{i,k}(P_{c,\mathrm{mx,ol},i}(k)^2)}, \quad i = 1, 2, \ldots, n_\mathrm{g} \tag{31}$$

with $P_{c,\mathrm{mx,cl},i}(k)$ and $P_{c,\mathrm{mx,ol},i}(k)$ being the closed- and open-loop simulations for the i^{th} gust half length. In Equation (31), the loads are squared in order to equally penalise negative and positive values. An optimal GLA controller minimises the maximum squared loads of the closed-loop system with respect to the open-loop system. Secondly, a constraint is applied on the relation between the closed-loop and open-loop maximum root mean square (RMS) of the WRBM [42]. This indirectly demands a certain decay rate for the closed-loop loads $P_{c,\mathrm{mx,cl},i}(k)$ after a gust encounter.

It is given by

$$c_{\text{rms}}(w_y, w_{\Delta u}) = \frac{\max\limits_i \left(\frac{1}{n_k} \sum_{k=1}^{n_k} P_{c,\text{mx,cl},i}(k, w_y, w_{\Delta u})^2 \right)}{\max\limits_i \left(\frac{1}{n_k} \sum_{k=1}^{n_k} P_{c,\text{mx,ol},i}(k)^2 \right)} \leq b_{\text{rms}}^2 \leq 1, \quad i = 1, \ldots, n_{\text{g}}. \tag{32}$$

The upper bound b_{rms} constrains the closed-loop RMS over all time steps n_k of the simulation. For the reference aircraft b_{rms} is $\sqrt{0.9}$ [43]. The optimisation is performed with a pattern search algorithm [44, 45].

C. Gust Load Alleviation Control Results

Controllers for MPC are defined for all 27 models. In Fig. 6 the effectiveness of the GLA controllers for mass case number five at different flight conditions is proven. The WRBM includes the increment that is induced by the gust

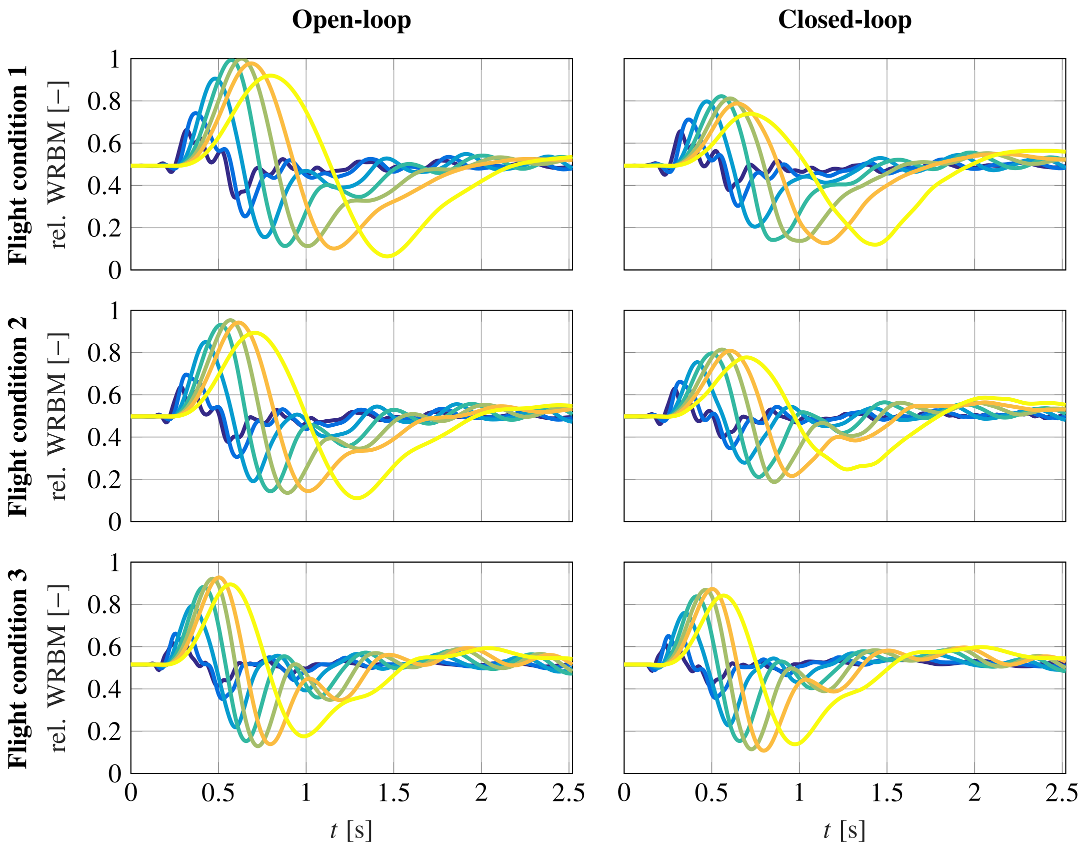

Fig. 6 Open- and closed-loop gust simulations of the relative WRBM of the reference aircraft for mass case 5 **and gust half lengths 9 m to 107 m.**

encounters plus the steady trim value. In this case the WRBM can be reduced by roughly 13 % between open- and closed-loop over all three flight conditions.

In order to judge what happens to the wing root torsional moment (WRTM) $P_{c,\text{my}}$ with respect to the WRBM $P_{c,\text{mx}}$, in Fig. 7 the maximum and minimum values of the WRTM are plotted over the maximum and minimum WRBM of the 189 performed simulations. The values for the WRBM and the WRTM are represented relative to the maximum open-loop WRBM over all considered cases. The grey diamond-shaped points depict the trim conditions, while the blue circles and the green triangles indicate the open- and closed-loop results. All three data sets are enclosed by their convex hull. As expected the maximum WRTM over the simulated gust encounters increases due to control surface

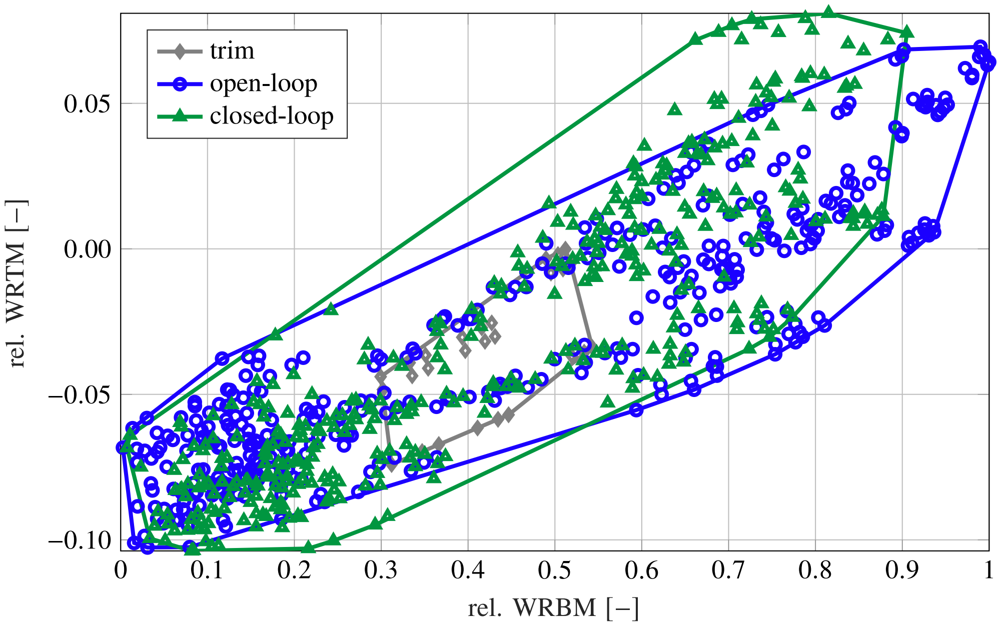

Fig. 7 Relative WRTM over relative WRBM.

deflection. However, it changes by around 1 %, which is not significant. The maximum WRBM can be reduced by 10 % between the open- and closed-loop case. The minimum values in the left bottom corner remain almost unchanged.

The WRBM can be reduced with GLA. However, when it comes to wing design, it is not enough to focus on the WRBM. Different positions along the wing have to be analysed. Therefore, for all gust simulations the BM at 39 positions between the wing root and wing tip is calculated. In Fig. 8 the relative BMs of the critical gust cases for the open-loop (top) and the closed-loop (bottom) are shown with respect to the relative wing span. The vertical dotted lines indicate the intermediate wing positions at which the BMs are calculated. The BM at each control point is put in correlation with the maximum open-loop BM that is observed at this control point over all 189 simulations. A relative BM equal to one denotes the gust case with the maximum expected BM. In the open-loop case the critical gust cases covering the maximum BM at all control points narrow down to four gust simulations, whereat the green and blue line almost match. The values m_i, f_i and H_i correspond to the indices of the mass configuration, the flight condition and the gust half length. For the open-loop system flying with high aircraft mass at low altitudes seems to be most critical with respect to gust loads. When GLA is applied five critical gust load cases are of relevance. Again, mainly maximum take-off or heavy payload mass cases at the lowest altitude are critical. The BMs are considered relative to the maximum BMs in open-loop, meaning values below one indicate an improvement with respect to the open-loop case. This is achieved for up to around 70 % of the wing span. Beyond this point the BM rises almost up to 40 % with respect to the open-loop system, which is undesirable when it comes to wing design. This phenomenon is caused by the ailerons on the outer wings which are deployed for GLA. Two steps will most likely lead to an improved behaviour in this regard. Firstly, more of the control surfaces distributed over the wings, like spoilers and flaps, should be deployed for GLA. Secondly, better adjustment of the input increment weights and introduction of a cost function penalising the absolute control surface deflections with respect to the bending moment at intermediate wing positions are assumed to improve the MPC design for GLA.

V. Conclusion and Outlook

A non-linear, aeroelastic model of a long-range aircraft is set up. The model is linearised for different mass cases and flight conditions. GLA controllers are synthesised for each linearised model with MPC, which solves an optimisation problem online. The cost function penalises certain sensor outputs, the WRBM estimated by a Kalman filter, and the increments in the deflections of the control surfaces allocated for GLA. The weights relating the different contributions to the cost function are determined through optimisation beforehand.

Based on the set of GLA controllers, the critical WRBM over all cases can be improved by 10 %. The increase in

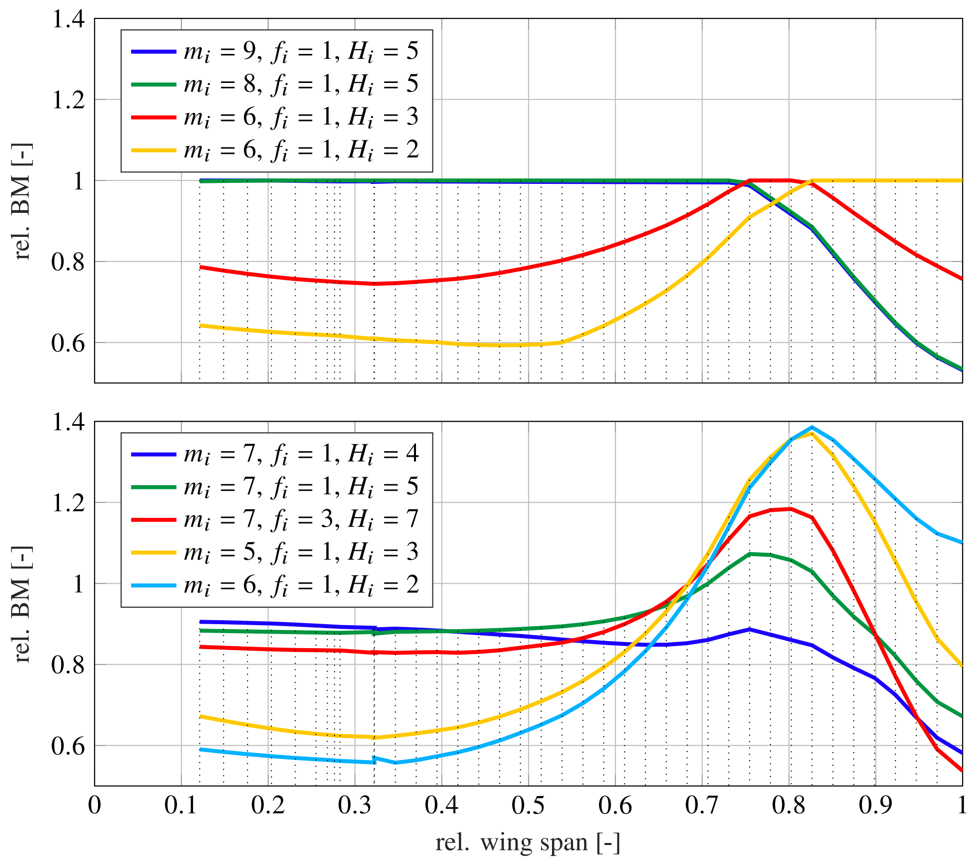

Fig. 8 Critical BM cases in open- (top) and closed-loop (bottom).

WRTM is insignificant. The examination of the BM along the wing, however, shows a sudden increase of the critical loads from 70 % span width onwards. This happens in the area where the ailerons deployed for GLA are located. The critical loads rise almost up to 40 % in comparison to the open-loop reference case. As a consequence, the reduction of gust induced loads needs to be more evenly distributed among more control surfaces along the wing. Using only the aileron and elevator control surfaces for GLA limits the possibility for lighter wing designs. Deploying spoilers or flaps would help to prevent such a strong increase in bending loads. Furthermore, the cost function solved with MPC has to be adjusted and augmented with respect to control inputs and their corresponding weights. For the adjustment of the weights it would be advantageous to take the BM at several intermediate wing positions into account.
As a GLA controller is synthesised for each individual mass case and flight condition, future research activities will focus on how to manage a stack of controllers and apply them corresponding to the state in which the aircraft is in.

Acknowledgments

The research leading to these results is part of the FLiPASED project. This project has received funding from the European Unions Horizon 2020 research and innovation program under grant agreement No. 815058.
Special thanks go to Reiko Müller, Özge Süelözgen, Simon Schulz and Thiemo Kier for inspiring discussions and valuable advices that made this work possible. Furthermore, I would like to thank my wife Silja, who has a talent for putting a smile on one's face.

References

[1] Jupp, J. A., "The design of future passenger aircraft – the environmental and fuel price challenges," *The Aeronautical Journal*, Vol. 120, No. 1223, 2016, pp. 37–60. https://doi.org/10.1017/aer.2015.4.

[2] Gössling, S., and Humpe, A., “The global scale, distribution and growth of aviation: Implications for climate change,” *Global Environmental Change*, Vol. 65, No. 1, 2020. https://doi.org/10.1016/j.gloenvcha.2020.102194.

[3] Livne, E., “Aircraft Active Flutter Suppression: State of the Art and Technology Maturation Needs,” *Journal of Aircraft*, Vol. 55, No. 1, 2018, pp. 410–452. https://doi.org/10.2514/1.C034442.

[4] Wright, J. R., and Cooper, J. E., *Introduction to Aircraft Aeroelasticity and Loads*, 2^{nd} ed., John Wiley & Sons, Ltd, Chichester UK, 2015.

[5] Regan, C. D., and Jutte, C. V., “Survey of Applications of Active Control Technology for Gust Alleviation and New Challenges for Lighter-weight Aircraft,” , No. DFRC-E-DAA-TN4736, 2012. URL https://ntrs.nasa.gov/citations/20120013450.

[6] Poussot-Vassal, C., Vuillemin, P., Cantinaud, O., and Sève, F., “Interpolatory Methods for Generic BizJet Gust Load Alleviation Function,” *SIAM Journal on Applied Dynamical Systems*, Vol. 20, No. 4, 2021, pp. 2391–2411. https://doi.org/10.1137/20M1384014.

[7] Binder, S., “Simultaneous Optimisation of Composite Wing Structures and Control Systems for Active and Passive Load Alleviation,” Dissertation, Delft University of Technology, Delft, 2021. https://doi.org/10.4233/UUID:FAC93CCF-7E0B-4971-A797-D2617E378A1D.

[8] Capello, E., Guglieri, G., and Quagliotti, F., “L1 Adaptive Controller Design for Gust Load Alleviation,” *29th Congress of the International Council of the Aeronautical Sciences (ICAS 2014)*, International Council of The Aeronautical Sciences (ICAS), 2014.

[9] Wüstenhagen, M., Ossmann, D., Poussot-Vassal, C., and Vuillemin, P., “Synthesis of a Multiple-Model Adaptive Gust Load Alleviation Controller for a Flexible Flutter Demonstrator,” *AIAA Scitech 2022 Forum*, American Institute of Aeronautics and Astronautics, Reston, Virginia, 2022, p. 4439. https://doi.org/10.2514/6.2022-0440.

[10] Kopf, M., Bullinger, E., Giesseler, H.-G., Adden, S., and Findeisen, R., “Model Predictive Control for Aircraft Load Alleviation: Opportunities and Challenges,” *2018 Annual American Control Conference (ACC)*, IEEE, 27.06.2018 - 29.06.2018, pp. 2417–2424. https://doi.org/10.23919/ACC.2018.8430956.

[11] Karpel, M., “Design for Active Flutter Suppression and Gust Alleviation Using State-Space Aeroelastic Modeling,” *Journal of Aircraft*, Vol. 19, No. 3, 1982, pp. 221–227. https://doi.org/10.2514/3.57379.

[12] Patil, M. J., and Hodges, D. H., “Output Feedback Control of the Nonlinear Aeroelastic Response of a Slender Wing,” *Journal of Guidance, Control, and Dynamics*, Vol. 25, No. 2, 2002, pp. 302–308. https://doi.org/10.2514/2.4882.

[13] McLean, D., and Prasad, R. A., “A structure load alleviation control system for a large aircraft,” *Transactions of the Institute of Measurement and Control*, Vol. 2, No. 1, 1980, pp. 25–37. https://doi.org/10.1177/014233128000200104.

[14] Dillsaver, M., Cesnik, C., and Kolmanovsky, I., “Gust Load Alleviation Control for Very Flexible Aircraft,” *AIAA Atmospheric Flight Mechanics Conference*, American Institute of Aeronautics and Astronautics, Reston, VA, 2011, p. 26. https://doi.org/10.2514/6.2011-6368.

[15] Zeng, J., Moulin, B., de Callafon, R., and Brenner, M. J., “Adaptive Feedforward Control for Gust Load Alleviation,” *Journal of Guidance, Control, and Dynamics*, Vol. 33, No. 3, 2010, pp. 862–872. https://doi.org/10.2514/1.46091.

[16] Giesseler, H.-G., Kopf, M., Varutti, P., Faulwasser, T., and Findeisen, R., “Model Predictive Control for Gust Load Alleviation,” *4th IFAC Conference on Nonlinear Model Predictive Control*, Vol. 45, 2012, pp. 27–32. https://doi.org/10.3182/20120823-5-NL-3013.00049.

[17] Fournier, H., Massioni, P., Pham, M. T., Bako, L., Vernay, R., and Colombo, M., “Robust Gust Load Alleviation at Different Flight Points and Mass configurations,” *AIAA SCITECH 2022 Forum*, American Institute of Aeronautics and Astronautics, Reston, Virginia, 2022. https://doi.org/10.2514/6.2022-0285.

[18] Fezans, N., Joos, H.-D., and Deiler, C., “Gust load alleviation for a long-range aircraft with and without anticipation,” *CEAS Aeronautical Journal*, Vol. 10, No. 4, 2019, pp. 1033–1057. https://doi.org/10.1007/s13272-019-00362-9.

[19] Fezans, N., Wallace, C., Kiehn, D., Cavaliere, D., and Vrancken, P., “Lidar-based Gust Load Alleviation - Results obtained on the Clean Sky 2 Load Alleviation Benchmark,” *International Forum on Aeroelasticity and Structural Dynamics 2022*, 2022.

[20] Cavaliere, D., and Fezans, N., “Recasting Discrete 1-Cosine Gust Load Criteria as Frequency-Domain Specifications for Load Alleviation Control Design,” *International Forum on Aeroelasticity and Structural Dynamics 2022*, 2022.

[21] Skogestad, S., and Postlethwaite, I., *Multivariable Feedback Control: Analysis and design*, 2$^{\text{nd}}$ ed., John Wiley and Sons, 2005.

[22] Raković, S. V., and Levine, W. S., *Handbook of Model Predictive Control*, Springer International Publishing, Cham, 2019. https://doi.org/10.1007/978-3-319-77489-3.

[23] Haghighat, S., Liu, H. H. T., and Martins, J. R. R. A., "Model-Predictive Gust Load Alleviation Controller for a Highly Flexible Aircraft," *Journal of Guidance, Control, and Dynamics*, Vol. 35, No. 6, 2012, pp. 1751–1766. https://doi.org/10.2514/1.57013.

[24] Artola, M., Goizueta, N., Wynn, A., and Palacios, R., "Aeroelastic Control and Estimation with a Minimal Nonlinear Modal Description," *AIAA Journal*, Vol. 59, No. 7, 2021, pp. 2697–2713. https://doi.org/10.2514/1.J060018.

[25] Wynn, A., Artola, M., and Palacios, R., "Nonlinear optimal control for gust load alleviation with a physics-constrained data-driven internal model," *AIAA SCITECH 2022 Forum*, American Institute of Aeronautics and Astronautics, Reston, Virginia, 01032022, p. 2019. https://doi.org/10.2514/6.2022-0442.

[26] Tewari, A., *Aeroservoelasticity: Modeling and Control*, Springer New York, New York, NY, 2015. https://doi.org/10.1007/978-1-4939-2368-7.

[27] GUYAN, R. J., "Reduction of stiffness and mass matrices," *AIAA Journal*, Vol. 3, No. 2, 1965, p. 380. https://doi.org/10.2514/3.2874.

[28] Kier, T., and Looye, G., "Unifying Manoeuvre and Gust Loads Analysis Models," *International Forum on Aeroelasticity and Structural Dynamics*, 2009.

[29] Wüstenhagen, M., Kier, T., Meddaikar, Y. M., Pusch, M., Ossmann, D., and Hermanutz, A., "Aeroservoelastic Modeling and Analysis of a Highly Flexible Flutter Demonstrator," *2018 Atmospheric Flight Mechanics Conference*, American Institute of Aeronautics and Astronautics, Reston, Virginia, 2018. https://doi.org/10.2514/6.2018-3150.

[30] Kier, T., and Hofstee, J., "Varloads - eine Simulationsumgebung zur Lastenberechnung eines voll flexiblen, freifliegenden Flugzeugs," *Deutscher Luft- und Raumfahrtkongress*, 2004.

[31] Wüstenhagen, M., Süelözgen, Ö., Ackermann, L., and Bartaševičius, J., "Validation and Update of an Aeroservoelastic Model based on Flight Test Data: 6-13 March 2021," *2021 IEEE Aerospace Conference (50100)*, IEEE, 2021. https://doi.org/10.1109/AERO50100.2021.9438354, URL https://ieeexplore.ieee.org/document/9438354.

[32] European Aviation Safety Agency, "Certification Specifications for Large Aeroplanes (CS-25)," 2007.

[33] Karpel, M., Moulin, B., and Chen, P. C., "Dynamic Response of Aeroservoelastic Systems to Gust Excitation," *Journal of Aircraft*, Vol. 42, No. 5, 2005, pp. 1264–1272. https://doi.org/10.2514/1.6678.

[34] Hanta, V., and Procházka, A., "Rational Approximation of Time Delay," 2009.

[35] Grauer, J. A., and Boucher, M. J., "Output Measurement Equations for Flexible Aircraft Flight Dynamics," , No. NASA/TM-2018-220102, 2018. URL https://ntrs.nasa.gov/citations/20180007917.

[36] Corda, S., *Introduction to aerospace engineering with a flight test perspective*, Aerospace series, Wiley, Chichester, West Sussex, 2017.

[37] Bisplinghoff, R. L., Ashley, H., and Halfman, R. L., *Aeroelasticity*, Dover Publications, Inc., 1955.

[38] Bemporad, A., Ricker, N. L., and Morari, M., "Model Predictive Control Toolbox Getting Started Guide," 2022. URL https://de.mathworks.com/help/pdf_doc/mpc/mpc_gs.pdf.

[39] Schwenzer, M., Ay, M., Bergs, T., and Abel, D., "Review on model predictive control: an engineering perspective," *The International Journal of Advanced Manufacturing Technology*, Vol. 117, No. 5-6, 2021, pp. 1327–1349. https://doi.org/10.1007/s00170-021-07682-3.

[40] Bemporad, A., Ricker, N. L., and Morari, M., "Model Predictive Control Toolbox User's Guide," 2022. URL https://de.mathworks.com/help/pdf_doc/mpc/mpc_ug.pdf.

[41] Varga, A., "Balancing Free Square-Root Algorithm for Computing Singular Perturbation Approximations," *30th Conference on Decision and Control*, Vol. 2, 1991, pp. 1062–1065.

[42] Rennie, R., and Law, J., *A dictionary of physics*, 6$^{\text{th}}$ ed., Oxford reference online premium, Oxford Univ. Press, Oxford, 2009.

[43] Wüstenhagen, M., "Model Selection for a Multiple-Model Adaptive Gust Load Alleviation Controller," *International Forum on Aeroelasticity and Structural Dynamics 2022*, 2022.

[44] Hooke, R., and Jeeves, T. A., ""Direct Search" Solution of Numerical and Statistical Problems," *Journal of the ACM*, Vol. 8, No. 2, 1960, pp. 212–229.

[45] Joos, H.-D., "A methodology for multi-objective design assessment and flight control synthesis tuning," *Aerospace Science and Technology*, Vol. 3, No. 3, 1999, pp. 161–176. https://doi.org/10.1016/S1270-9638(99)80040-6.